Acta Biomaterialia xxx (xxxx) xxx

Contents lists available at ScienceDirect

Acta Biomaterialia

journal homepage: www.elsevier.com/locate/actbio

Full length article

Nanoscale geometry determines mechanical biocompatibility of vertically aligned nanofibers

Samuel Rantataro[a], Ilmari Parkkinen[b,c], Ishan Pande[a], Andrii Domanskyi[b], Mikko Airavaara[c,d], Emilia Peltola[a,e], Tomi Laurila[a,f,*]

[a] Department of Electrical Engineering and Automation, Aalto University, Maarintie 8, Espoo, 02150, Finland
[b] Institute of Biotechnology, HiLife, University of Helsinki, Biocenter 2, Helsinki, 00014, Finland
[c] Division of Pharmacology and Pharmacotherapy, Faculty of Pharmacy, University of Helsinki, Viikinkaari 5E, Helsinki, 00014, Finland
[d] Neuroscience Center, HiLife, University of Helsinki, Biomedicum 1, Haartmaninkatu 8, Helsinki, 00014, Finland
[e] Department of Mechanical and Materials Engineering, University of Turku, Vesilinnantie 5, 20100 Turku, Finland
[f] Department of Chemistry and Materials Science, Aalto University, Kemistintie 1, Espoo, 02150, Finland

ARTICLE INFO

Article history:
Received 25 October 2021
Revised 11 April 2022
Accepted 20 April 2022
Available online xxx

Keywords:
Mechanical biocompatibility
Astrocyte
Carbon nanofiber
Focal adhesion
Atomic force microscopy

ABSTRACT

Vertically aligned carbon nanofibers (VACNFs) are promising material candidates for neural biosensors due to their ability to detect neurotransmitters in physiological concentrations. However, the expected high rigidity of CNFs could induce mechanical mismatch with the brain tissue, eliciting formation of a glial scar around the electrode and thus loss of functionality. We have evaluated mechanical biocompatibility of VACNFs by growing nickel-catalyzed carbon nanofibers of different lengths and inter-fiber distances. Long nanofibers with large inter-fiber distance prevented maturation of focal adhesions, thus constraining cells from obtaining a highly spread morphology that is observed when astrocytes are being contacted with stiff materials commonly used in neural implants. A silicon nanopillar array with 500 nm inter-pillar distance was used to reveal that this inhibition of focal adhesion maturation occurs due to the surface nanoscale geometry, more precisely the inter-fiber distance. Live cell atomic force microscopy was used to confirm astrocytes being significantly softer on the long Ni-CNFs compared to other surfaces, including a soft gelatin hydrogel. We also observed hippocampal neurons to mature and form synaptic contacts when being cultured on both long and short carbon nanofibers, without having to use any adhesive proteins or a glial monoculture, indicating high cytocompatibility of the material also with neuronal population. In contrast, neurons cultured on a planar tetrahedral amorphous carbon sample showed immature neurites and indications of early-stage apoptosis. Our results demonstrate that mechanical biocompatibility of biomaterials is greatly affected by their nanoscale surface geometry, which provides means for controlling how the materials and their mechanical properties are perceived by the cells.

Statement of significance

Our research article shows, how nanoscale surface geometry determines mechanical biocompatibility of apparently stiff materials. Specifically, astrocytes were prevented from obtaining highly spread morphology when their adhesion site maturation was inhibited, showing similar morphology on nominally stiff vertically aligned carbon fiber (VACNF) substrates as when being cultured on ultrasoft surfaces. Furthermore, hippocampal neurons matured well and formed synapses on these carbon nanofibers, indicating high biocompatibility of the materials. Interestingly, the same VACNF materials that were used in this study have earlier also been proven to be capable for electrophysiological recordings and sensing neurotransmitters at physiological concentrations with ultra-high sensitivity and selectivity, thus providing a platform for future neural probes or smart culturing surfaces with superior sensing performance and biocompatibility.

* Corresponding author.
E-mail address: tomi.laurila@aalto.fi (T. Laurila).

https://doi.org/10.1016/j.actbio.2022.04.032
1742-7061/

1. Introduction

Most neural electrodes are made from highly rigid materials, even when intended for *in vivo* measurements. This elicits a mechanical mismatch with the nervous tissue and activates both microglia and astrocytes [1], contributing to formation of a detrimental glial scar around the electrode and eventually insulating it from target neurons, thus rendering the electrode dysfunctional [2].

While the specific mechanism of glial scarring around an implant remains largely unknown, the ability of cells to probe surface mechanics is thought to have a pivotal role in it [1]. The principle for mechanosensing is based on cell-generated contractile forces into actin cytoskeleton and transmitting them to the substratum through cell adhesion sites [3,4], after which the surface rigidity is gauged by stress-activating adhesome proteins [5]. Because vinculin is one of the main constituents of the force-transducing layer of cell adhesome [5], presence of the mechanosensory machinery can be evaluated based on vinculin immunostaining. Vinculin is also present in mature focal adhesions (FA), whose development requires actomyosin-mediated forces and if they are not present, the adhesion site disassembles [5].

Cell adhesion sites contain integrins that are clustered together. Integrin clustering requires individual integrins to be closer than ≈70 nm apart [6], whereas the width of individual adhesive patch must also be sufficiently large to fit at least two integrins [7] whose subunit heads have a diameter of ≈8-12 nm [8]. Considering these limitations and knowing nascent adhesions being consisted of ≈50 integrins [9], minimum size for adhesion patches can be calculated to be ≈400x20 nm (length x width) or ≈100 nm diameter circle when RGD is used as the integrin binding ligand. If the size of adhesion patches does not meet these minimum requirements, only short-lived adhesion sites are formed [7] that is indicated by inhibition of maturation into FAs [10]. This would further prevent the formation of stress fibers.

If the size of individual adhesion patches is sufficiently large, cell adhesion can mature over distances larger than that required for integrin clustering. Thus, the cell adhesome ”bridges” over non-adhesive regime, which has been observed to occur when the inter-patch distance is small enough [11]. According to the data obtained by Malmström et al. [11], adhesion sites were incapable to bridge over the distance of ≈100 nm when the adhesive patch diameter was 100 nm (lengths measured by us according to their figures). This indicates that small adhesion sites, including nascent adhesions, follow the 70-nm rule of integrin clustering. In contrast, significant bridging behavior can be observed when cells are cultured on larger adhesive patches, although there appears to be a maximum distance over which bridging is not possible anymore [11].

Cell adhesion can thus be controlled by surface geometry and more importantly, the nanoscale geometry. Because cell adhesion plays major role in the mechanosensory machinery of cells, preventing cell adhesion can be used to deceive cells to perceive stiff surfaces as if they were soft. Preventing the maturation of cell adhesion also inhibits cytoskeletal tensile stress, restraining the cells from obtaining highly spread morphology and also rendering them soft that would not otherwise occur on non-patterned stiff surfaces.

Here in this study, we aimed to present design rules for controlling the mechanical biocompatibility of apparently stiff surfaces. We also show that a wafer-scale non-lithographic manufacturing process can be used to grow VACNFs that meet these design rules. VACNFs were also examined for their neuronal biocompatibility in order to identify whether they could be used *in vivo* or *in vitro* in the future.

2. Materials and methods

2.1. Preparation of culture substrates

2.1.1. Glass coverslip

Glass coverslips (12 mm diameter, Thermo Scientific) that were used with astrocytes were sterilized by autoclaving at 134 °C prior to being coated with laminin. Coverslips (VWR) used with hippocampal neurons were first treated overnight in 70% nitric acid (Sigma-Aldrich), then sterilized in autoclave, and lastly coated overnight with 0.5 mg/mL poly-l-ornithine and washed thrice with PBS prior to using with cells.

2.1.2. Hydrogel

Gelatin hydrogel was manufactured with a previously introduced protocol [12] under sterile conditions. Type A porcine gelatin (300 Bloom; G1890, Sigma-Aldrich) was dissolved into sterile-filtered deionized water (DIW) to produce 8% (g/mL) solution, which was pre-heated to 50°C before sterilization through 0.22-µm filter. Microbial transglutaminase (*mTg*, ACTIVA WM, Ajinomoto) was dissolved into sterile DIW at 37 °C to produce 8% (g/mL) solution, which was then filter-sterilized. Gelatin solution was mixed at a 1:1 ratio with mTg solution, and this 4% (g/mL) gelatin-mTg mixture was then administered in 1 mm thickness onto tissue-culture treated polystyrene 60 mm dishes (*TCP*, Corning), or onto glass coverslip for cell staining. The hydrogel was crosslinked overnight in room temperature, after which it was sterilized for 20 minutes under ultraviolet illumination. Prior to being coated with laminin, the hydrogel was re-hydrated with phosphate buffered saline (*PBS*; 21-031-CV, Corning) for 5 minutes.

2.1.3. Carbon nanomaterials

Long Ni-CNF samples were fabricated using a previously reported method [13]. Briefly, 20 nm of titanium was sputtered onto p-type boron doped Si $<100>$ wafer ($R < 0.005$ ohm-cm) (Siegert Wafer, Germany), after which 7 nm of tetrahedral amorphous carbon (ta-C) was grown with filtered cathodic vacuum arc deposition. Processing for the ta-C sample ended here, while processing was continued for the long Ni-CNF sample in the following manner. A 20-nm thick nickel catalyst layer was grown with the cathodic arc deposition without breaking the vacuum. The samples were then moved to another chamber and annealed for 3-minutes at 400 °C, and then plasma-enhanced chemical vapor deposition (PECVD, Black Magic, AIXTRON) was used to grow the fibers in 750 °C for 30 minutes in the same chamber, using C_2H_2 (30 SCCM) as a precursor in combination with NH_3 (125 SCCM) gas.

The samples with *short* Ni-CNFs had same type of silicon wafer, while they received 80 nm of evaporated chromium adhesion layer and 20 nm of evaporated nickel as the catalyst layer. The samples were then brought to the PECVD chamber and fibers were grown in 600 °C for 10 minutes without annealing, using C_2H_2 (30 SCCM) as a precursor in combination with NH_3 (125 SCCM) gas.

All carbon nanomaterials were sterilized by autoclaving at 134 °C.

2.1.4. Silicon nanopillars

P-type boron doped Si $<100>$ wafer ($R < 0.005$ ohm-cm) was selected. Polymethyl methacrylate (PMMA) 950 A resist (KayakuAM, USA) was patterned with standard electron beam lithography process to contain holes of 200 nm diameter that were arranged into a hexagonal array on 250x250 µm area (Supplementary Fig. S1), having a gap of either 100 nm or 500 nm between each circle. Aluminum was evaporated at 20 nm thickness onto the PMMA pattern, after which lift-off was done in acetone. This

produced a hard mask with 200 nm diameter circles of aluminum. Silicon was dry etched with a cryogenic process at -110 °C using SF_6/O_2 chemistry in Plasmalab 100 (Oxford Instruments, UK) tool.

Silicon nanopillar samples were sterilized by autoclaving at 134 °C. Samples were moved to a 12 well plate and 3 mL of PBS was added to the wells, after which samples were incubated overnight at 37 °C under humidified and 5.0% CO_2 atmosphere. Laminin coating was prepared on the samples prior to seeding cells.

2.1.5. Laminin coating

Laminin coating was used with astrocyte cultures only. Mouse laminin (354232, Corning) was dissolved according to the manufacturer's guidance, after which it was diluted into Minimum Essential Medium (M2279, Sigma-Aldrich) at a 10 μg/mL concentration. This diluted solution was used as such on the glass coverslips, Ni-CNF samples, and silicon nanopillars. Laminin was crosslinked onto the gelatin hydrogel by mixing the laminin solution at a 1:1 ratio with sterile 4% mTg solution, as introduced previously [12]. The substrates were incubated at 37 °C under humidified and 5.0% CO_2 atmosphere for 1 h. After incubation, the substrates were washed twice with PBS and were then used immediately.

2.2. Cell culture

2.2.1. Primary cell culture preparation

NMRI mice were housed at a 12-hour light-dark cycle, with water and food *ad libitum*. All animal experiments were approved by the Finnish National Board of Animal Experiments (license number: ESAVI/13959/2019) and performed according to the European legislation on the protection of animals used for scientific purposes. Astrocyte cultures were obtained from one dissection, whereas neuronal cultures were prepared from two dissections.

Astrocyte cultures were prepared, in part, using the David Sulzer laboratory ventral midbrain culture "glia preparation" protocol [14]. The cortices of 2-day-old mice were dissected, the meninges and hippocampus were removed before cutting the cortices into small pieces and treated with papain for glia solution (Sulzer lab ventral midbrain culture protocol) for 10 minutes. The pieces were washed with M10C-G medium, triturated with a siliconized glass Pasteur pipette in M10C-G, centrifuged for 5 min at 1000 RPM, plated into Greiner T25 cell culture flasks (Sigma-Aldrich) and maintained in a humidified incubator (37 °C, 5% CO_2, saturated humidity, RH 80–100%). After 2 hours, the partially adhered cells (non-glia) were detached from the flask mechanically. The cells were washed twice with cold minimum essential medium (Sigma-Aldrich) and the floating cells were aspirated. After washing, cold M10C-G was added, and flasks were placed back into the incubator. After astrocytes reached approximately 70–80% confluency (3–5 days), FDU-solution (6.7 μg/mL 5-fluorodeoxyuridine and 16.5 μg/mL uridine) (Sigma-Aldrich) was added for mitotic inhibition. After 7 days, cells were washed with PBS and trypsinized. Cells were resuspended in M10C-G, centrifuged for 5 min at 1000 RPM and resuspended into freezing medium containing M10C-G, 20% Fetal Bovine Serum (Sigma-Aldrich), and 10% dimethyl sulfoxide. Cells were placed into freezing vials and were frozen gradually (1 °C/1 min) in a -80 °C freezer. The vials were placed into a liquid nitrogen tank on the following day.

2.2.2. Astrocyte culture

All cell culturing procedures were conducted under sterile conditions. Complete culturing medium (M10C-G) was freshly prepared. Cortical astrocytes (Passage 2) were thawed rapidly in 37 °C water bath. The vial contents (1 mL) were transferred into 9 mL of pre-heated complete medium and centrifugated at 51.8 RFC for 5 minutes. Cells were then resuspended into complete growth medium and seeded at 20 000 cells/cm^2 density onto each of the culturing substrate types, all of which had a freshly prepared laminin coating. Cultures were incubated in 37 °C temperature-controlled incubator under humidified and 5.0% CO_2 atmosphere. Cultures were washed once with PBS on the following day, after which fresh pre-heated complete medium was added and the cultures were placed back into incubator.

Double-staining for vinculin and actin on glass coverslip, Ni-CNF samples, and gelatin hydrogel had similar culturing protocol than described above, except cells were subcultured once and seeded at a density of 2 400 cells/cm^2.

2.2.3. Neuron culture

Animal care and license were presented in Section 2.2.1. Hippocampi were dissected from the brains of 4-day-old mice, cut into pieces and treated with papain for neurons solution for 10 minutes. The neuron-containing pieces were washed with Neurobasal-A medium (NB-A) (Sigma-Aldrich), triturated with a siliconized glass Pasteur pipette in NB-A, centrifuged for 5 min at 1000 RPM, after which cells were plated into a plastic 12-well Greiner CellStar plate (Sigma-Aldrich) containing the following samples *without* laminin coating: long Ni-CNF (1×10^6 cells/well), short Ni-CNF (5×10^6 cells/well), and ta-C (1×10^6 cells/well). Poly-l-ornithine coated glass coverslip worked as a cytocompatible control sample, that was freshly prepared prior to seeding cells (5×10^6 cells/well). Neurons were cultured in NB-A medium (Gibco) supplemented with 2% B27 (Gibco), 40 μM L-glutamine (Sigma-Aldrich), and 1% penicillin, streptomycin and maintained in humidified incubator (37 °C, 5% CO_2, saturated humidity, RH 80–100%). On the following day, FDU-solution was added to the cultures for mitotic inhibition of the glia. Half of the culture media supplemented with FDU-solution was changed 4 days after seeding.

2.3. Atomic force microscopy

Mechanical property measurements were carried out by using a Dimension Icon AFM (Bruker Inc) in Force Volume mode. Two types of probes were used. Because sharp indenters are known to produce local strains in hydrogels and result into excessively large elastic modulus estimations [15], we selected a large probe to obtain area-averaged elastic modulus values from each indented location on the samples. A novel hemispherical 5-μm radius probe on MLCT lever (Bruker Inc, Pat. No. 10,802,045) was used to measure elastic modulus of the gelatin hydrogel and vertical CNF samples. In contrast, live cell measurements were conducted with a 17-μm tall conical PeakForce QNM Live Cell probe (PFQNM-LC-A-CAL, Bruker Inc) that has 17.5° half-opening angle and 70 nm tip radius, being small enough to identify elastic modulus differences between specific cellular regions.

Before any measurements were conducted, the probes were calibrated. Spring constants of both probe types were pre-calibrated by the manufacturer, being 0.065 N/m for the hemispherical probe in hydrogel measurements and 0.333 N/m in vertical CNF measurements, while the live-cell probes had spring constant between 0.09-0.103 N/m. Deflection sensitivity was calibrated for both probe types in their respective measurement fluids according to the manufacturer's protocol: mean average value was calculated according to 5 indentation curves obtained from an infinitely stiff surface (glass coverslip or silicon wafer). This calculation was automatically done by NanoScope software (Bruker Inc).

2.3.1. Characterization of hydrogel

In total, 12 replica hydrogel samples were manufactured from 3 different batches with the previously mentioned protocol, and were then coated with laminin. Samples were washed twice with

PBS, after which minimum essential medium (M2279, Sigma-Aldrich) supplemented by 10% fetal bovine serum (Gibco) was added to the dishes. Next, the dishes were incubated at 37 °C under humidified and 5.0% CO_2 atmosphere for 2 hours to obtain equilibrium state in the hydrogel. The hydrogel samples were washed once with PBS prior to adding the measurement liquid, that was PBS, to the samples. Samples were stored inside the incubator until being measured. Samples were brought to atomic force microscope (AFM) and indentation measurements were performed at 37 °C temperature, measuring 2 randomly selected locations from each hydrogel sample.

Each measurement location consisted of a 60 μm x 60 μm area with 16 equally spaced indentation points, producing in total 32 data points from an individual sample. The most important measurement parameters that may influence the shape of force curve and thus apparent elastic modulus, were selected as follows: Ramp Size (2 μm), Forward Velocity (4 μm/s), Reverse Velocity (4 μm/s), and Threshold value (10 nN).

Force curves obtained from the hydrogel samples were analyzed with Hertzian contact model [16,17]. When assuming the indenting sphere having infinitely large elastic modulus compared to the sample and the sample having infinite dimensions, along with several other assumptions [18], applied force F can be related to indentation by the following equation:

$$F = \frac{4}{3}\frac{E_{sample}}{(1-\nu^2)} * \delta^{\frac{3}{2}}\sqrt{R} \quad (1)$$

, where ν is the Poisson ratio of sample, δ is indentation depth, and R is the sphere radius. E_{sample} denotes the apparent elastic modulus of the sample. Poisson ratio of 0.5 was selected for the hydrogel, as it is commonly used for gelatin [19,20].

2.3.2. Characterization of vertical CNFs

Long and *short* Ni-CNF samples were characterized with AFM in air atmosphere. Both sample types were measured from three locations, each consisting of a 40 x 40 μm area with 16 equally spaced indentation points. Measurement parameters were similar in both sample types and were selected as follows: Ramp Size (500 nm), Forward Velocity (1 μm/s), Reverse Velocity (1 μm/s), and Threshold value of (10 nN).

Force curves were analyzed with the Hertzian contact model. Poisson ratio of 0.25 was selected for both long and short CNFs based on the literature data [21].

2.3.3. Cell mechanics of cortical astrocytes

Astrocytes were cultured for two days prior to measuring them with AFM. Cell mechanical measurements were performed onto individual cultures (N = 4–6) of each sample type. All cultures were gently washed once with PBS. Cell-containing glass coverslip and both Ni-CNF sample types were then transferred onto TCP dishes (Corning). Pre-heated complete medium was then added to all dishes, which were placed into incubator until being brought to the AFM. A heater stage was connected to temperature controller system (Model 335, LakeShore) that was used to maintain the culture at 37 °C temperature throughout the measurements. Because the culture was exposed to ambient atmosphere without 5% CO_2 during the measurement, all the captured data was taken in less than 2 hours to prevent excess alkalinity shift from inducing changes to the cells.

AFM was used to characterize apparent elastic modulus of cortical astrocytes (N = 20 each sample type) on glass coverslip, 4% gelatin hydrogel, *long* Ni-CNFs, and *short* Ni-CNFs. As the tip radius was only 70 nm, force curves were captured from individual locations from all cell regions. The most important measurement parameters were selected as follows: Ramp Size (2.50 μm), Forward Velocity (31.3 μm/s), Reverse Velocity (31.3 μm/s), and Threshold value (600 pN). Force curves obtained from living cells were analyzed with the Sneddon model for conical indenters [22,23], according to which applied force F is related to indentation by:

$$F = \frac{2}{\pi}\frac{E_{cell}}{(1-\nu^2)} * \delta^2 tan(\alpha) \quad (2)$$

, where ν is the Poisson ratio of sample, δ is indentation depth, α is the half-opening angle of the conical AFM tip, and E_{cell} is the apparent elastic modulus at the measurement location. Poisson ratio of 0.5 was selected, which is a commonly chosen estimate value for biological samples [24] and is very close to the actually measured value for NIH3T3 cells [25].

2.3.4. Data processing

Nanoscope Analysis software (Bruker Inc) was used to implement Hertzian (samples) or Sneddon (living astrocytes) contact mechanical model on the force curves. Contact points were automatically determined by the Nanoscope Analysis software (Bruker Inc), which uses a linearized fit model for the force curve analysis. Force Fit boundaries were set between 15.0% and 60.0% to obtain best fit to the data for astrocytes on all culturing substrate types. Elastic modulus data maps were stored and then processed in Gwyddion software (Gwyddion 2.56, Open-Source software) to exclude extracellular regions and outliers. Data points with invalid force curves were removed manually. All the valid data points were transferred to Prism 9.0 software (GraphPad) and mean average of each cell was used for statistical analysis.

Data analysis for the hydrogel samples contained Force Fit boundaries between 40.0–80.0%, or alternatively the fit boundaries were selected manually if autofitting was incorrect. For the vertical CNF samples, fit boundaries were selected manually. Apparent elastic modulus values from each indentation point were then transferred to Prism software.

2.4. Immunofluorescence

2.4.1. Cortical astrocyte culture

Cultures were washed thrice with PBS between each of the following steps, unless otherwise noted. Astrocytes were grown on culturing substrates at 2 400 cells/cm^2 density for 66 hours, being then fixed with 4% paraformaldehyde (PFA) in PBS for 20 minutes at room temperature (RT). After permeabilization with 0.5% Triton X-100 in PBS solution for 10 minutes, cells were blocked with 10% normal goat serum (G9023, Sigma-Aldrich) in 0.1% bovine serum albumin in PBS solution (BSA-PBS) for 1 h. The cultures were washed once with 0.5% Triton X-100 solution, and then incubated in mouse monoclonal anti-vinculin antibody (V9131, Sigma-Aldrich) at 1:200 dilution in BSA-PBS at RT for 1 h. Samples were washed three times with 0.5% Triton X-100 solution. Secondary goat anti-mouse antibody conjugated to Alexa-488 (A-11001, Thermo Fisher) at 1:400 dilution and Phalloidin conjugated to CF568 (00044, Biotium) at 1:30 dilution in BSA-PBS were added to the samples for 1 h at RT. The staining protocol for short Ni-CNF sample was similar, except samples were incubated for 1h 15 min with the primary vinculin antibody and were washed twice with PBS and once with 0.5% Triton X-100 solution prior to adding Alexa-488 conjugated secondary antibody that was used at 1:200 dilution. Samples were coverslipped with DAPI-containing mounting medium (H-1200, Vector Laboratories).

Astrocytes were cultured on the silicon nanopillar samples for 48 hours prior to fixing with 4% PFA in PBS solution for 20 minutes at room temperature. Cells were permeabilized with 0.5% Triton X-100 in PBS solution for 10 minutes, after which they were washed once with PBS and then twice with 0.1% Triton X-100 in PBS solution. After this, the staining protocol was identical with the short Ni-CNF sample.

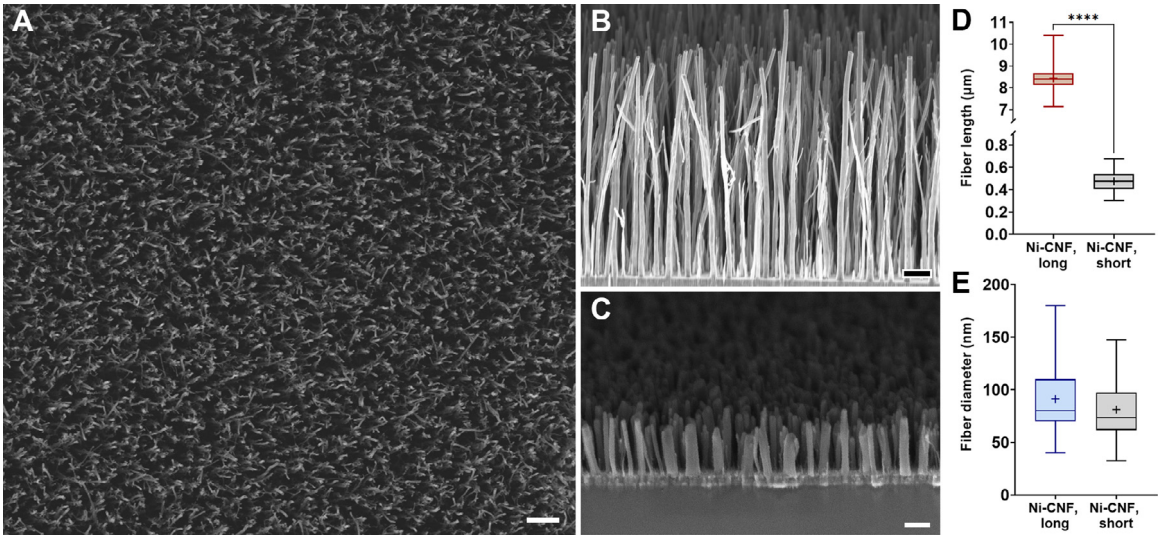

Fig. 1. Top-view of the long Ni-CNF sample (A) and 75° angle side-view scanning electron micrographs of the long (B) and short (C) Ni-CNF samples. Scale bar in figure (A) is 2 μm, (B) 1 μm, and (C) 250 nm. Fiber length analysis (D) shows most fibers having length between 8.15-8.60 μm in the long-fiber sample, and 0.40-0.55 μm in the short-fiber sample. (N = 50) Fiber length was significantly different on these two samples (****$p < 0.0001$). Mean averages are denoted as +. Fiber diameter analysis (E) shows most of the fibers having diameter between 70–110 nm in the long-fiber sample, and 60–100 nm in the short-fiber sample. (N = 75). The difference in fiber diameter between long and short Ni-CNFs was not statistically significant.

Images from fluorescently stained samples were captured through Nikon Plan Apo (10x) or Plan Fluor EPI (20x, 50x) air objectives using Nikon DS-Fi3 camera that was connected to an upright microscope (Nikon Eclipse-E). An antireflective black-silicon wafer was used below the microscope slides. Images were processed by using the following image-processing tools in NIS-Elements AR Analysis software (Nikon) to enhance details, which would otherwise be difficult to distinguish due to background color: "General Convolution", "Adjust Details and Noise via Fourier Transform", "Component contrast", and background subtraction. Original images are available at our data repository file.

2.4.2. Focal adhesion analysis

The size of FAs was analyzed from 10 astrocytes on all sample types (Supplementary Fig. S9), each image captured from their own field. Post-processing and quantitative analysis was based on the protocol introduced in Horzum et al. [26] but modified slightly. Processing protocol in the present study was done with ImageJ using the following functions, accordingly: Subtract Background (rolling ball radius 100 pixels, Sliding paraboloid) → CLAHE (25 block size, 256 histogram bins, 6 maximum slope) → Adjust Brightness & Contrast (Auto) → Math Exp → Threshold → Analyze particles from 0.15 μm^2 to infinity, with circularity 0.00-0.99. This protocol automatically selected FAs and calculated their area, after which the values were analyzed with Prism 9.0 (GraphPad, USA).

2.4.3. Hippocampal neuron culture

After culturing for 10 days *in vitro*, neurons were fixed with 4% PFA for 20 minutes at RT, permeabilized with 0.2% Triton X-100 for 15 min at RT and blocked with 0.2% Triton X-100 and 5% normal horse serum (NHS) for 1h at RT, both in PBS. The cells were stained with 200 ng/ml DAPI in PBS for 10 min at RT, anti-NeuN (MAB377, Sigma-Aldrich), anti-MAP2 (ab5392, Abcam) and anti-Synaptophysin (101002, Synaptic Systems) primary antibodies and anti-mouse AF647 (A32787, ThermoFisher), anti-chicken AF568 (ab175477, Abcam) and anti-rabbit AF488 (A21206, ThermoFisher) secondary antibodies. Stainings were done all sequentially 1st primary then 1st secondary, for 1h at RT with 3 x PBS washed in between antibody incubations. All antibodies were diluted 1:500 in 0.2% Triton X-100 and 5% NHS in PBS.

Samples were placed on glass microscope slides and cover-slipped with Fluoromount-G (SouthernBiotech) mounting medium. Samples were imaged with a Zeiss LSM 880 confocal microscope through a 10x air objective using single plane 3x3 tile imaging and with a 63x (NA 1.3) oil objective for a Z-stack of singular neurons. Images were acquired using the same channel settings for all samples. Tile images were stitched using ImageJ/FIJI (National Institutes of Health) stitching plugin, Z-stacks were maximum intensity projected and all images were pseudocolored with no additional image manipulations using ImageJ. For the four low-magnification images (Supplementary Fig. S13-S16), background colors were processed away with ImageJ.

2.5. Statistical methods

The number of cells to be measured was evaluated based on the Mead's resource equation [27], where the degree of freedom for error term (DF) should be between 10 and 20 to provide adequate information without using excess resources [28]. Given that we had four different sample types, measuring 20 cells from each of them yields DF to be 16.

Anderson-Darling test was first performed to evaluate normality of the data sets. Statistical significance was tested for Ni-CNF length and diameter data (Fig. 1) and elastic modulus data (Supplementary Fig. S3) with nonparametric two-tailed Mann-Whitney test. Focal adhesion size data (Supplementary Fig. S9) was analyzed with nested One-way ANOVA, whereas astrocyte mechanical measurement data (Fig. 2) was analyzed with a nonparametric Kruskal-Wallis test. The data are plotted as box and whisker plots when applicable. Line within the box indicates median value and box boundaries contain 50% (25-75%) of all data points, while whiskers denote the minimum and maximum values within each group. In the text, all values were reported as the mean average ± standard deviation.

3. Results

3.1. Characterization of samples

Physical properties of samples used in this study are summarized in Table 1, including aspect ratio (length/diameter) for the

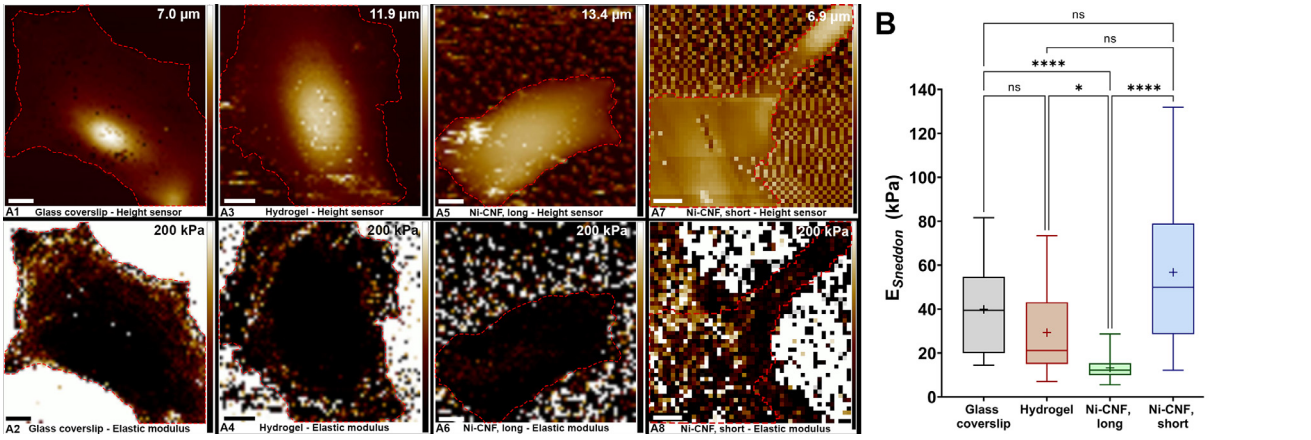

Fig. 2. (A) AFM height sensor data and elastic modulus maps obtained from cortical astrocytes on glass coverslip (A1,2), gelatin hydrogel (A3,4), and long (A5,6) or short (A7,8) Ni-CNFs. Dashed red line denotes cell edges and thus the area for data selection. Scale bar is 10 µm, while the color scale is either height or elastic modulus depending on image type. (B) Apparent elastic modulus of astrocytes on four culturing substrates, cells being significantly softer when cultured on the long Ni-CNF sample (N = 20 cells from each sample type). ****p < 0.0001, *p = 0.0155. Mean average is denoted as + for the cells, being 39.87 kPa on glass coverslip, 29.32 kPa on hydrogel, 13.22 kPa on *long* Ni-CNF, and 56.76 kPa on *short* Ni-CNF samples. (For interpretation of the references to colour in this figure legend, the reader is referred to the web version of this article.)

Table 1
Physical properties of the different sample types. Glass coverslip, gelatin hydrogel, and ta-C are planar samples.

	Length	Diameter	Aspect Ratio	Elastic modulus	Spring constant
Glass coverslip	-	-	-	63.7 ± 0.3 GPa Ref. [30]	-
Gelatin hydrogel	-	-	-	11.39 ± 2.03 kPa	-
Ni-CNF, long	8.44 ± 0.62 µm	91 ± 30 nm	92.7	9.29 ± 9.41 MPa	0.156 pN/µm
Ni-CNF, short	0.48 ± 0.09 µm	81 ± 26 nm	5.93	31.34 ± 30.0 MPa	1800 pN/µm
ta-C	-	-	-	310-790 GPa Ref. [31,32]	-
Si nanopillar, 100 nm gap	3.81 ± 0.04 µm	188.5 ± 2.9 nm	20.2	130 GPa Ref. [33]	437 nN/µm
Si nanopillar, 500 nm gap	3.50 ± 0.06 µm	188.6 ± 3.2 nm	18.6	130 GPa Ref. [33]	565 nN/µm

vertically aligned nanofibers. Spring constants (K) were calculated according to the Euler-Bernoulli beam theory approximation [29], where $K = 3\pi Ed^4/(64L^3)$. Elastic modulus (E) in the equation was measured for the Ni-CNF samples with AFM, whereas literature value was chosen for the silicon nanopillars.

3.1.1. Characterization of vertically aligned CNFs

The overall morphology of Ni-CNF samples was characterized by scanning electron microscopy (SEM) (Fig. 1). Typical length of the fiber was between 8.2–8.6 µm for long Ni-CNFs (Fig. 1.D), the average fiber having a length of 8.44 ± 0.62 µm. These fibers were significantly longer (****p < 0.0001) than on the short Ni-CNF sample, where average fiber length was 0.48 ± 0.09 µm. Most of the fibers on both sample types had a diameter between 60–110 nm (Fig. 1.E), the average fiber diameter being 91 ± 30 nm for long Ni-CNF samples and 81 ± 26 nm for short Ni-CNF samples. There was no significant difference (p = 0.0617) in the fiber diameter between these two samples. These fiber length and diameter averages yield an aspect ratio of 92.7 for the long Ni-CNF sample, which is very high. In contrast, the aspect ratio for short Ni-CNFs was only 5.93.

The distance between neighboring Ni-CNFs was measured based on scanning electron micrographs (Supplementary Fig. S17-S19). The average distance to a nearest neighboring fiber was 494.4 ± 208.0 nm for the *long* Ni-CNF sample and 147.1 ± 36.3 nm for the *short* Ni-CNF sample. When measured from three neighboring fibers, the average inter-fiber distance was 700.6 ± 189.8 nm for the *long* Ni-CNF sample and 178.8 ± 33.4 nm for the *short* Ni-CNF sample. In both measurement protocols, there was a significant difference in the inter-fiber distances (****p < 0.0001).

Elastic modulus of the Ni-CNF samples was analyzed by AFM. Elastic modulus for the long Ni-CNF sample was 9.29 ± 9.41 MPa, being significantly softer than the short Ni-CNF sample (****p < 0.0001) (Supplementary Fig. S3).

3.1.2. Characterization of gelatin hydrogel

We observed that mixing 4% (g/mL) gelatin solution with 8% mTg solution yielded cracks in the hydrogel (data not shown). To obtain a homogeneous surface, we prepared gelatin-mTg mixture from 8% gelatin solution that yielded final gelatin concentration of 4% (g/mL). Indentation experiments were performed with an AFM onto 12 individual samples of this 4% gelatin hydrogel. Elastic modulus of the hydrogel was measured to be 11.39 ± 2.03 kPa (Supplementary Fig. S4). This is closely resembling that of the elastic modulus obtained for 8% gelatin hydrogel elsewhere [12]. While the gelatin concentration of our hydrogel was only half of that in Ref. [12], the observed increase in elastic modulus of our hydrogels was expected because of larger gelatin Bloom number (300 vs. 175).

3.1.3. Characterization of silicon nanopillars

After dry etching, silicon nanopillar samples were characterized with SEM to verify that the sample can accurately control adhesion site location. In principle, cell adhesion can form in any location with collapsed pillars because it would remove the gap between adjacent pillars. Our 100 nm gap pillar sample was describing a situation, where adhesion site maturation was not inhibited and recapitulated a similar situation as the short Ni-CNF sample. Because of this, having few collapsed pillars in the 100 nm gap sample does not prevent using the sample. In contrast, collapsed pillars

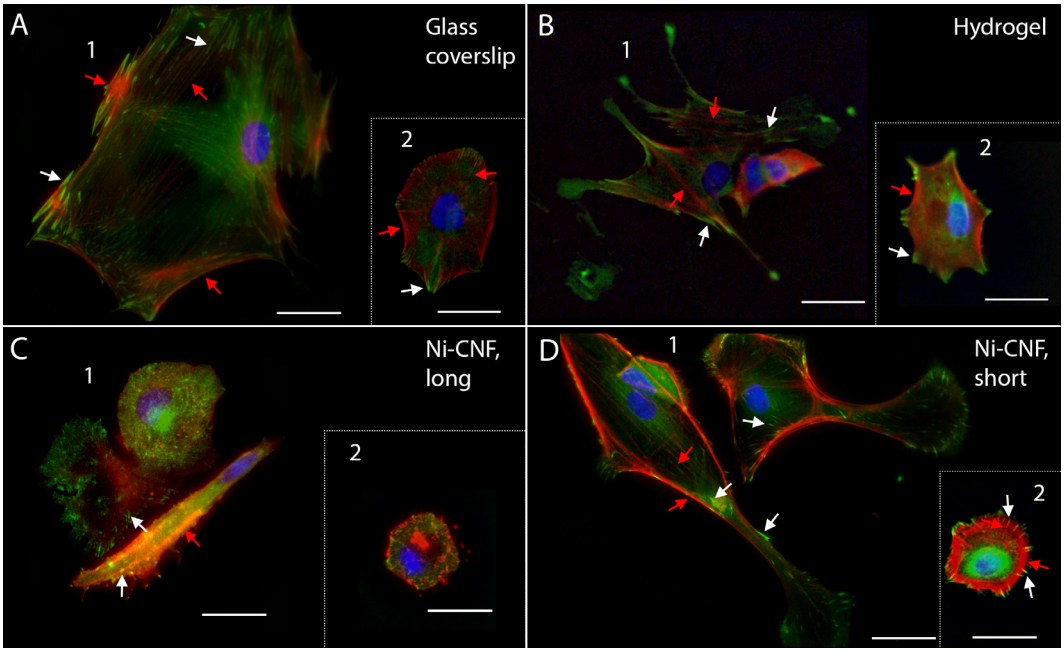

Fig. 3. Cortical astrocytes were immunostained for vinculin (green), actin (red), and DAPI (blue). Cells were seeded at 2 400 cells/cm^2. Mature FAs (white arrows) and actin stress fibers (red arrows) were observed in large quantities on glass coverslip (a), hydrogel (b), and short Ni-CNF samples (d). Astrocytes on long Ni-CNFs (c) showed only individual FAs in random orientation, and either lacked stress fibers completely or showed them only at the cell periphery. Large and small cells were imaged from different fields. Non-linear processing was used to enhance details over background in the figures. Scale bar is 20 μm. (For interpretation of the references to colour in this figure legend, the reader is referred to the web version of this article.)

in the 500 nm gap sample would render the sample unusable. Accordingly, we used a 100 nm gap sample that had few collapsed pillars and a pristine 500 nm gap sample (Supplementary Fig. S2).

Because the pillar sidewall images were captured at a 25° angle, length of the pillars was calculated according to the following equation:

$$L_{Real} = \frac{L_{Measured}}{sin(25^{\circ})} \quad (3)$$

, where L_{Real} is the actual length of pillars and $L_{Measured}$ is the measured length according to SEM images. Length L_{Real} of the pillars on 100 nm gap sample was 3.81 ± 0.04 μm, whereas 3.50 ± 0.06 μm on the sample with 500 nm gap between individual pillars (N = 20).

3.2. Characterization of cortical astrocytes

3.2.1. Atomic force microscopy

Culturing time of two days was chosen to ensure maturation of cell adhesion sites and allowing reorganization of the cytoskeleton according to the cell-material interactions. When astrocytes were characterized by AFM, the culturing medium underwent a gradual alkalinity shift (data not shown) because the measurements were conducted in ambient air without 5% CO_2. An increase in alkalinity is known to increase dissociation rate of actin [34], while it is also known to regulate actomyosin activity [35] and is thus expected to affect cytoskeletal tensile stresses [36]. According to the tensegrity theory [37], a decrease in cytoskeletal tensile stress can be observed as a decrease in apparent elastic modulus [38]. Because we did not observe any correlation between the time under measurement conditions and apparent elastic modulus of astrocytes (Supplementary Fig. S5-S8), we can conclude our data gathering time window (2 hours) to be sufficiently small to prevent any harm from occurring to the cells.

Cortical astrocytes were observed to be significantly softer when cultured on long Ni-CNFs compared to being on glass coverslip (****$p < 0.0001$) or hydrogel (*$p = 0.0155$) (Fig. 2.B). Contrasting this, when astrocytes were cultured on *short* Ni-CNFs where FA maturation was not blocked (Fig. 3.D), there was no significant difference in cell stiffness when compared to glass coverslip ($p > 0.9999$) or hydrogel sample ($p = 0.0796$) (Fig. 2.B). We also did not observe significant difference between cells cultured on hydrogel sample or glass coverslip ($p = 0.7347$), although the cells were slightly softer on hydrogel. Similar conclusion can be made when comparing all the force curves that were captured from one cell on each sample type (Supplementary Fig. S10).

3.2.2. Immunofluorescence of cortical astrocytes

Focal adhesions can be detected by the combination of a strong vinculin fluorescence signal, elongated shape of the structure, and being located at the end of actin stress fibers [39]. Astrocytes showed mature FAs in large quantities on glass coverslip, hydrogel, and short Ni-CNF samples (Fig. 3). In contrast, astrocytes on the *long* Ni-CNF sample showed mostly dotlike nascent adhesions or focal complexes and only few individual FAs. In addition, cells on the *long* Ni-CNF sample lacked long and strongly labeled adhesion sites in the central region of the cells that were observed on other sample types, which would presumably be fibrillar adhesions [39].

Stress fibers are thick actin-containing bundles that can be distinguished from actin filaments by their size but also more importantly, their anchorage to FAs [40]. Stress fibers are evidently seen in all the large cells in Fig. 3, with the exception of cells on the *long* Ni-CNF sample. Actin filament bundles may also be organized into curved transverse arc structures [40], which is evident in the smaller cell on *short* Ni-CNF sample (Fig. 3.D). Absence of stress fibers in astrocytes cultured on long Ni-CNFs can be explained by the small size of FAs (Supplementary Fig. S9) and their almost random orientation in relation to each other (Fig. 3.C), as the formation of stress fibers requires mature FAs [41]. Preventing the maturation of adhesion sites by vertical nanostructures has also been reported elsewhere for various non-neural cell types [42,43], although differences between cell types were observed.

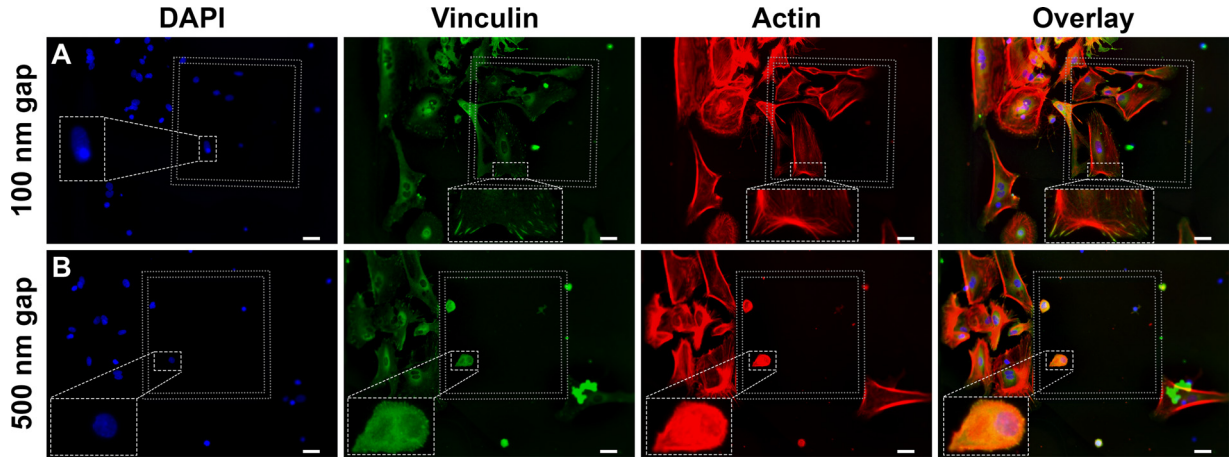

Fig. 4. Primary astrocytes (20 000 cells/cm^2) cultured on 200 nm diameter silicon pillars with inter-pillar gap of 100 nm (row A) or 500 nm (row B). Patterned area is present within the inner gray square. Adhesion sites of the cells mature similarly on 100 nm gap sample compared to the neighboring flat surface, whereas adhesion is incapable of maturing when the inter-pillar gap is 500 nm. Non-linear processing was used to enhance details over background in the figures. Scale bar is 20 μm.

When comparing cellular morphology, we observed cells being highly spread on glass coverslip, hydrogel, and short Ni-CNF substrates (Fig. 3 and Supplementary Fig. S11). Maintenance of this well-spread morphology requires tensile stress that is induced by stress fibers, most notably peripheral stress fibers [44]. On the long Ni-CNF substrate however, actin filament organization into stress fibers was inhibited (Fig. 3.C) and only a minority of cells were able take a large and well-spread morphology (Supplementary Fig. S12). Response of astrocytes to the long Ni-CNF substrate appeared highly similar to being cultured on ultrasoft gels, stress fibers being unable to form and astrocytes remaining rounded [45]. Because our fiber growth process has stochastic nature, it was not surprising that the long Ni-CNF sample also contained a few locations where the fibers were positioned closer to one another and thus the cell could spread.

3.2.3. Adhesion bridging

In order to decouple the effect of inter-fiber distance and Ni-CNF length on adhesion maturation, we cultured cortical astrocytes on silicon nanopillars with their inter-pillar gap being either 100 nm or 500 nm (Fig. 4). We observed adhesion sites to mature on the 100 nm gap pattern similarly compared to cells on the planar surface that was present outside the patterned area. In contrast, adhesion site maturation was completely prevented on the sample with 500 nm inter-pillar gap. Accordingly, astrocytes were highly spread on the 100 nm gap pattern but remained small and had a spherical morphology on the 500 nm gap pattern.

3.3. Viability of hippocampal neurons on VACNFs

In order to determine whether vertically aligned carbon nanofibers could be used *in vivo* or as a smart culturing substrate, we evaluated their cytompatibility with hippocampal neurons. A poly-L-ornithine coated glass coverslip functioned as a positive control sample, whereas a ta-C coated silicon wafer worked as a reference planar sample to determine whether carbonaceous surface itself would increase neural cytocompatibility (Fig. 5 and Supplementary Fig. S13-S16).

Both long and short Ni-CNF samples showed viable neurons after ten days *in vitro*. Similarly to the control glass coverslip, neurons cultured on the Ni-CNF samples grew long and arborized dendrites with mature synapse-forming neurons, as is shown by the NeuN, MAP2 and synaptophysin markers (Fig. 5 and Supplementary Fig. S13-S15). In contrast, the planar ta-C samples contained smaller number of neurons with condensed nuclei (Supplementary Fig. S16), which together with the observation of retracted neurites indicates poor survival of neurons. This highlights that carbonaceous surface itself does not significantly increase neuronal cytocompatibility but instead, it requires a specific nanoscale surface geometry that is present in the vertically aligned CNFs.

4. Discussion

Vertically aligned, long and sparsely distributed Ni-CNFs were shown to inhibit maturation of FAs and thus the organization of actin cytoskeleton. This was clearly observed from the immunofluorescence images, and our cell mechanics measurements provided further supporting evidence by showing astrocytes being significantly softer on the long Ni-CNF samples compared to other substrate types. It has earlier been postulated that rigid substrates can be nanopatterned to inhibit geometrical maturation of adhesion sites and thus make the substrates mimic the responses caused by soft matrices [46], which is consistent with the results from our study.

4.1. Cell adhesion maturation

The distance between individual nanofibers in the long Ni-CNF sample was larger than 70 nm that would be required for integrin clustering, and the distance can range up to 1.7 μm (Supplementary Fig. S17). Because of that, we expected this nanostructure to prevent longitudinal clustering of integrins between individual CNFs. In addition, the fiber diameter is close to the minimum patch size for nascent adhesions (Fig. 1.E). These facts together could explain why adhesion sites remained small and mostly spherical, which is typical for nascent adhesions [9] and focal complexes [47]. Few adhesion sites were however able to mature up to the typical size of FAs (Supplementary Fig. S9), which may develop on locations where individual fibers are clustered together in random locations due to stochasticity of the manufacturing process (Supplementary Fig. S20).

Cell adhesion sites have been observed to mature over non-adhesive regimes when the inter-patch distance is sufficiently small [11]. Although adhesion bridging occurs more prominently with larger adhesive patches, there is a maximum distance over which bridging is not possible anymore. We observed this also in some cells cultured on long Ni-CNFs, where individual vinculin-stained spherical adhesion sites were observed close to one another (Fig. 3.C and Supplementary Fig. S22). In contrast, majority of the short Ni-CNF sample surface contained fiber “clusters” with

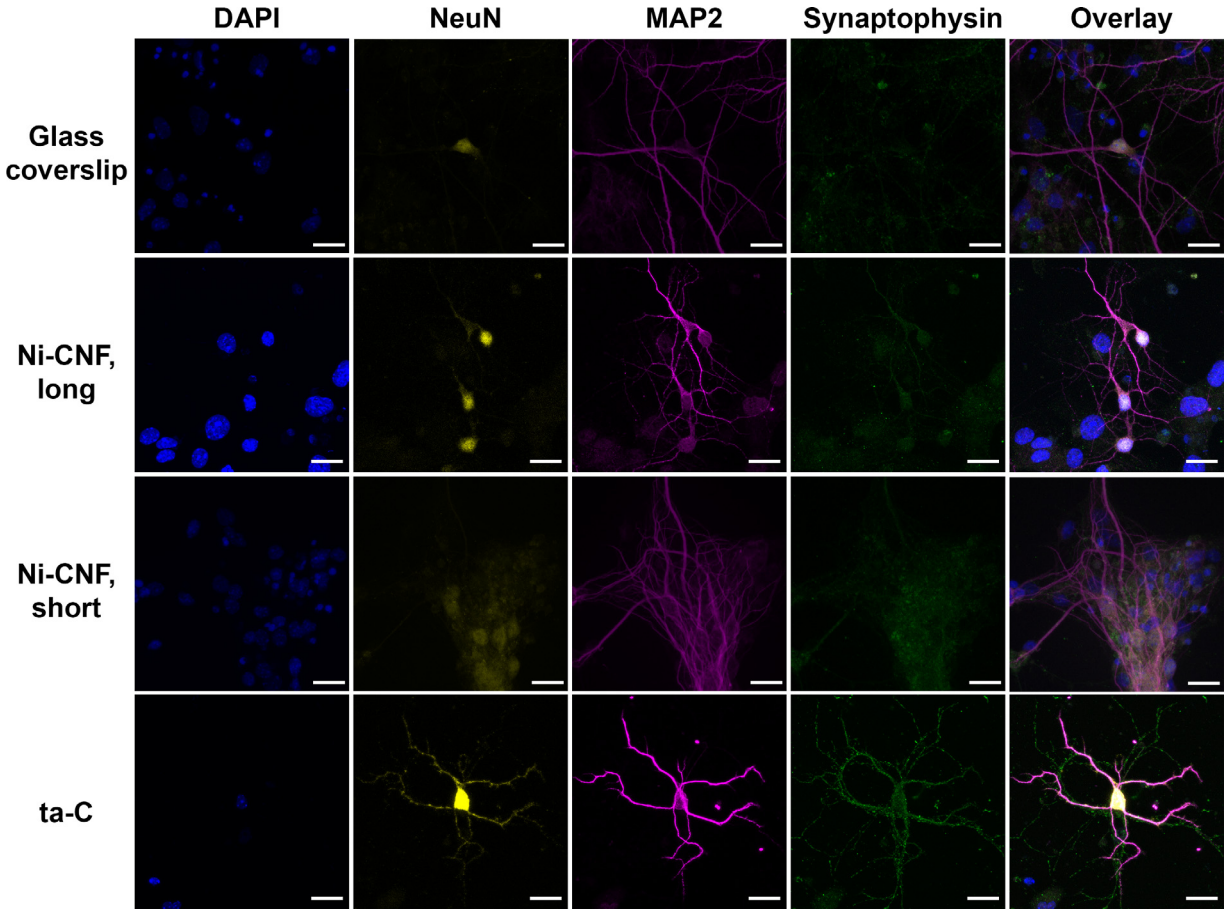

Fig. 5. Hippocampal neurons cultured on different surfaces. Cells were immunostained to detect neurons (NeuN, yellow), dendrites (MAP2, magenta) and presynapses (Synaptophysin, green), and were counterstained with DAPI (blue) to visualize the nucleus. Scale bar is 20 μm. (For interpretation of the references to colour in this figure legend, the reader is referred to the web version of this article.)

inter-fiber distances ranging between 120–170 nm (Supplementary Fig. S17), and thus it was not surprising to observe adhesion site bridging over these small inter-fiber spaces.

We hypothesize adhesion bridging to occur through talin protein that can be stretched by cytoskeletal tensile stress up to the lateral length of 350 nm [48], into which vinculin can then bind to and stabilize the adhesion site [48,49]. Although bridging has been observed to increase the length of adhesion sites, their width remains restricted by the adhesive pattern (Figure S4 in Ref. [11]). We also observed this on the long Ni-CNF sample, where the few longer adhesion sites remained very narrow (Supplementary Fig. S22). This provides further support for talin being the fundamental bridging element, as the tensile force that is stretching talin occurs along the axis of stressed actin filament [50]. Adhesion bridging was prevented on the *long* Ni-CNF sample when the distance between individual adhesion sites exceeded 350 nm (Supplementary Fig. S22), which was replicating the behavior on silicon nanopillars with accurately controlled 500 nm inter-pillar distance where adhesion bridging was completely prevented. Lastly, it is important to note that the adhesive ligand [11] and cell type [11,51] both may affect the critical dimensions for adhesion maturation.

An earlier study by Li et al. [52] showed the maximum cellular traction force being approximately 12.5 nN for non-cancerous cells that were cultured on GaInP nanopillars with following dimensions: diameter of 104 nm, length of 2.6 μm, and inter-pillar distance of 760 nm (measured by us based on their figures). Assuming that traction force scales linearly as a function of adhesion point area [53] also on the nanoscale, cells on our 188 nm diameter silicon nanopillars would show theoretical maximum traction force of approximately 41 nN, a force that is capable of causing lateral bending of 72 nm to the silicon nanopillars. Our silicon nanopillars can thus be thought to be excessively stiff for the cells.

When the lateral bending of silicon nanopillars by cellular traction forces is also considered, the theoretical minimum for inter-pillar distance would be 356 nm on our 500 nm gap silicon nanopillar sample, thus being above the talin stretching limitation. By considering this fact while noting the exceedingly high spring constant (565 nN/μm) of silicon nanopillars, we conclude that inter-pillar distance is more important than spring constant in dictating the adhesion site maturation on vertically aligned nanopillars or nanofibers.

By preventing the adhesion site maturation, also the organization of actin cytoskeleton is inhibited. This was clearly observed in the silicon nanopillar experiment, where astrocytes on the 100 nm inter-pillar distance sample showed significant amount of stress fibers, without distinction to the neighboring flat surface area. By contrast, astrocytes on the 500 nm inter-pillar distance sample lacked stress fibers and most of the actin was concentrated onto cell periphery, replicating the results obtained earlier by Li et al. [52] with epithelial cells on their 760 nm inter-pillar distance samples. Thus, the organization of actin cytoskeleton on vertically aligned nanostructures appears to be a general cellular phenomena not limited to astrocytes only. Unfortunately, the other researchers did not target cell adhesion molecules in their immunofluorescence experiments [52].

When seeding is done from a homogeneous cell suspension, one may assume an even distribution of cells on the sample surface. Thus, some of the cells will land onto patterned area with the silicon nanopillars, whereas other cells land onto the neighboring non-patterned area (Fig. 4). Because of this, we can evaluate differences in FA formation from the same cell population on patterned area and flat area. Although cells would be capable of migrating from patterned area to flat area (or vice versa), immunofluorescence staining remains to show differences in cells that are present on these two areas at the time point of fixation. Hence, our experimental set-up does not study cellular migration but instead, it is used to study differences in FA maturation on different surface geometries.

We must note here that the silicon nanopillar samples also contained a 10-μm wide "moat" structure between patterned area and flat area, with depth of the moat being similar to the nanopillar height. This moat was designed to inhibit cell migration. As is shown by the results, the moat worked as intended and restricted cells onto the edges of moat, with the exception of two cells on 100-nm gap pattern sample (Fig. 4.A). Because the nuclear region of these two cells was either directly on top of the moat or touching the edge of moat, we expect that these two cells landed onto the moat and thus were initially extended on both sides of the moat. On the 500-nm gap sample (Fig. 4.B), we did not observe any cells extending into the moat from neither the patterned area or neighboring flat area.

4.2. Cell mechanics and actin cytoskeleton

Our cell mechanical experiment results are also well lined with literature data [54,55], showing apparent elastic modulus or stiffness of cells to correlate with an increase in F-actin or its organization into stress fibers (Fig. 2.B and Fig. 3). Cytoskeletal organization is accommodated with an increase in cytoskeletal tension, which can be observed by stiffening of the cells [56,57]. There was no significant difference in the $E_{Sneddon}$ between cortical astrocytes cultured on glass coverslip, hydrogel or short Ni-CNFs, highlighting similarities in the organization of stress fibers and cellular spreading on these three substrates (Fig. 3.A,B,D). In contrast, astrocytes cultured on the long Ni-CNF substrate were shown to contain stress fibers mostly on the cell periphery only (Fig. 3.C).

Although the apparent elastic moduli ($E_{Sneddon}$) were larger than usually reported (2–20 kPa) in the literature for living astrocytes [58,59] and other cell types [60], our data fits into similar range than obtained in other studies for astrocytes [61–63]. We must highlight that the indentation velocity in our measurements was high (31.3 μm/s), which is known [64–66] to increase the measured apparent elastic modulus value. In such situation, cytosolic fluid does not have time to move in relation to the cytoskeleton [66] and the cells can be though to behave almost as a mechanically fully incompressible material [64]. Nevertheless, our interest lies more on the *relative* differences between astrocytes cultured on the four distinct substrates instead of obtaining absolute elastic modulus values from cells on each substrate type.

Morphological differences between astrocytes on the *long* Ni-CNFs and other sample types are reminiscent of earlier studies [1,45], where astrocytes were shown to remain in spherical morphology when cultured on compliant (100–200 Pa) polyacrylamide surfaces, while stiffer (9–10 kPa) substrates induced significant spreading that is characteristic for reactive astrocytes. Note that these modulus values for polyacrylamide substrates were reported as shear modulus, which translate into elastic modulus values of approximately 300–600 Pa and 26.6–29.6 kPa when Poisson ratio of 0.48 is selected [67]. Transition of astrocytes towards a more spread morphology initiates on gels slightly below elastic modulus of 3 kPa and saturates above 6 kPa [45,67]. As the elastic modulus of our gelatin hydrogel (11.39 ± 2.03 kPa) was above this saturation level, it is not surprising that both the cellular morphologies and apparent elastic moduli were highly similar on hydrogel samples and glass coverslips or *short* Ni-CNFs.

Changes in cell area and actin organization are usually accompanied by increased cellular tensile forces [56,68,69] that must be opposed according to Newton's third law of motion. In highly spread cells, the majority of compressive stresses are transmitted to the substratum to bear [70] through FAs. Restricting the size of adhesion sites thus limits cytoskeletal tensile stresses [53] and via that also cell spreading. Accordingly, cortical astrocytes lacked organization of the actin cytoskeleton and remained mostly in rounded morphology when cultured on the *long* Ni-CNF substrate. Cells also appeared significantly softer when cultured on the *long* Ni-CNFs, providing further evidence for decreased cytoskeletal prestress.

To further demonstrate the effect of long Ni-CNFs on cortical astrocytes, we compared the cytoskeletal organization in non-spread cells. These non-spread astrocytes developed centripetally oriented stress fibers on glass (Fig. 3.A_2) and short Ni-CNFs (Fig. 3.D_2), while there was no clear orientational preference of actin cytoskeleton on long Ni-CNFs (Fig. 3.C_2). This behavior was highly similar to cells being cultured on an ultrasoft substrate. We expect this behavior to occurr due to limiting FA maturation, as the cells on the 500 nm gap silicon nanopillars showed similar response than on long Ni-CNFs. Because the formation of a dense glial scar requires spreading of astrocytes, we hypothesize electrodes with vertically aligned nanostructures to also inhibit glial scarring when the nanoscale geometry is designed to prevent adhesion site maturation. However, this requires further investigation.

4.3. Biocompatibility of Ni-CNFs

For the material to prevent glial scarring or to function as a culturing substrate, matching the surface mechanics alone is not sufficient because the material also has to be biocompatible. Thus, we evaluated cytocompatibility of the selected electrode materials by culturing hippocampal neurons on them. Neurons were observed to be viable on the Ni-CNF samples after 10 days *in vitro* and formed synapses, which indicates high biocompatibility of the sample materials. This observation was based on the immunocytochemical markers (NeuN, MAP2, Synaptophysin) and morphological characteristics of the neurons [71]. Although MAP2 has been generally considered to be a neuronal dendritic marker, it was recently found that MAP2 can also be detected in glial progenitors when embryonic mouse cortical cultures are used [72]. However, as our cultures were extracted from more developed postnatal mouse brains and we also detected NeuN in the same cells, it is more reliable to conclude that these cells were indeed neurons [73], although a further assessment of specific glutamatergic neuron markers, such as VGLUT2 [74], would have been optimal. The functionality of synapses in terms of electrophysiological activity remains unclear as the density and time of culture affects maturation of neurons [75] and thus should be further assessed by appropriate methods, such as patch clamping [76,77]. Overall, it was a significant finding that neurons remained viable without using surface coating protocols or providing trophic support by a nearby glia monolayer culture, as is typically [71,78] required. In contrast to the vertically aligned CNF samples, neurons cultured on planar ta-C sample were comparable to low-density cultures or cultures devoid of growth factors, i.e. they had immature neurites and less cells altogether [79]. This could arise from the minimal surface roughness (1.18 ± 0.02 nm, Supplementary Fig. S23) on the ta-C sample, which has been observed elsewhere for untreated silicon surfaces [80] to affect neuronal viability negatively.

Lastly, we must consider the effect of nickel because it is known to have toxic effect through disrupting homeostasis for physiological ions (Mg^{2+}, Ca^{2+}) [81] and inducing oxidative stress for cells [82]. Although nickel is known to dissolve into physiological-like saline solutions at pH 7.4 [83], we must emphasize that nickel content in our samples is very small due to the catalyst layer thickness being only 20 nm. This yields a total nickel content of approximately 18 μg for our sample pieces, of which less than 1% may dissolve during the first 24 hours according to data obtained with artificial interstitial fluid [83]. Furthermore, the total dissolved nickel content is likely to be significantly smaller, as the dissolution profile is expected to be similar to bulk nickel because the nanoparticles are conserved at the nanofiber tips and protected from the sides by carbon sheets, and the exposed areas are at least partly passivated by oxide layer already after fabrication [84]. In addition to the aforementioned factors, astrocytes secrete antioxidants to protect neurons from oxidative stress and thus the antioxidant level in astrocytes is expected to be higher than in neurons [85,86]. As neurons are more sensitive to oxidative stress than astrocytes [87] and neurons were observed in the present study to cope well on both long and short Ni-CNFs, we conclude that the effect of Ni-CNFs on adhesion site maturation and morphology of cortical astrocytes cannot be due to dissolving nickel. This is strongly supported by the fact that we observed similar limitations to adhesion site maturation on silicon nanopillars that are chemically very inert and different compared to the Ni-CNFs.

5. Conclusion

Vertically aligned CNFs are materials capable of highly sensitive electrochemical detection of neurotransmitters, while their mechanical biocompatibility with neural cells has remained unclear. While the geometrical softening of beam-like structures has already been studied elsewhere for other cell types, we addressed the combination of geometrical softening and effect of nanoscale topography on cell adhesion with neural cells for the first time. Our data suggests that there is a well-defined maximum distance, over which adhesion sites are incapable of maturing over. This in turn limits the organization of actin cytoskeleton and thus affects cell spreading and migration, while potentially also affects mechanosensory pathways of the cells.

Because diffusion of neurotransmitters towards the implant surface is greatly inhibited by a dense and thick glial scar [88,89], inhibiting its formation would improve the longevity of electrochemical sensors *in vivo*. By preventing the astrocytes from obtaining mature adhesion sites, the ability of cells to spread is constrained and they remain soft and rounded. This would suggest that a thick and dense glial scar could not be formed in the implant's near vicinity, however it would have to be verified *in vivo*.

We grew long, vertically aligned Ni-CNFs with their diameters small enough and inter-fiber distance sufficiently large to prevent formation of mature FAs, which effectively inhibited cortical astrocytes from obtaining a highly spread morphology that is required for a dense glial scar. We observed hindered organization of the actin cytoskeleton, which was reminiscent to other studies where astrocytes are cultured on ultrasoft surfaces [45]. In contrast, closely packed short Ni-CNFs with similar fiber diameters did not inhibit FA organization, and cells appeared similar to those cultured on glass coverslips. We also used atomic force microscopy to show astrocytes being significantly softer when cultured on the long and sparsely distributed Ni-CNFs, compared to samples where adhesion maturation was not inhibited, including a soft gelatin hydrogel. This further confirmed disorganization of the actin cytoskeleton, which was apparent from immunofluorescence images.

Because the long Ni-CNFs had much smaller spring constant compared to short Ni-CNFs, the effect of inter-fiber distance on FA maturation had to be decoupled from fiber length. We manufactured high-stiffness silicon nanopillars with similar inter-fiber distances as was observed for the long and short Ni-CNFs. Maturation of FAs was completely prevented when the distance between adjacent silicon pillars was 500 nm, resembling the results obtained with long Ni-CNF samples. In contrast, 100 nm inter-pillar distance did not prevent FA maturation and cells appeared similar to those cultured on planar surface or short Ni-CNF sample.

Bearing in mind these cell mechanical aspects while noting the fact that vertically aligned CNFs have been succesfully used in electrophysiological measurements [90] as well as in detection of dopamine [91] and glutamate [92] in physiological concentrations, electrodes made from these CNFs could potentially be used for long-term neural interfacing and neurotransmitter concentration measurement applications. More importantly, the same electrode could be used to both stimulate nearby neurons and then measure their neurotransmitter releasing events, which could possibly be used in adaptive DBS stimulation implants [93] that are used for treating neurological diseases such as Parkinson's [94]. Alternatively, vertical CNF electrodes could potentially be used *in vitro* as a smart culturing substrate for neurons that would be capable of sensing neurotransmitters, in addition to producing and recording electrical signals because the fibers are electrically conductive.

Data availability

The raw data required to reproduce these findings alongside with our data processing file are available to download from [Rantataro, Samuel (2022), "Nanoscale Geometry determines Mechanical Biocompatibility of Vertically Aligned Nanofibers", Mendeley Data, V1, doi:10.17632/8pw5zt94d4.1].

Declaration of Competing Interest

The authors declare no conflict of interest.

Acknowledgments and funding

We wish to thank MSc Jarkko Etula for kindly providing us the ta-C containing samples, and PhD Toni Pasanen for kindly providing us the antireflective black silicon material that was used in upright fluorescence imaging. We wish to also thank PhD Christoffer Kauppinen for sharing his knowledge in lift-off processing, and PhD Ali Shah for great discussion and sharing his expertise in cryogenic etching. We acknowledge the provision of facilities by Aalto University at OtaNano - Micronova Nanofabrication Centre and we would also like to thank the Biomedicum Imaging Unit (BIU), Helsinki, for microscopy services. This work was supported by European Union's Horizon 2020 research and innovation programme H2020-FETPROACT-2018-01 (No. 824070), Academy of Finland (No. 321996 and No. 328854), and Jane and Aatos Erkko Foundation.

Supplementary material

Supplementary material associated with this article can be found, in the online version, at doi:10.1016/j.actbio.2022.04.032

References

[1] P. Moshayedi, G. Ng, J.C. Kwok, G.S. Yeo, C.E. Bryant, J.W. Fawcett, K. Franze, J. Guck, The relationship between glial cell mechanosensitivity and foreign body reactions in the central nervous system, Biomaterials 35 (13) (2014) 3919–3925, doi:10.1016/j.biomaterials.2014.01.038.
[2] J.W. Salatino, K.A. Ludwig, T.D. Kozai, E.K. Purcell, Glial responses to implanted electrodes in the brain, Nat. Biomed. Eng. 1 (11) (2017) 862–877, doi:10.1038/s41551-017-0154-1.

[3] D.E. Discher, P. Janmey, Y.L. Wang, Tissue cells feel and respond to the stiffness of their substrate, Science 310 (5751) (2005) 1139–1143, doi:10.1126/science.1116995.
[4] A.J. Engler, S. Sen, H.L. Sweeney, D.E. Discher, Matrix elasticity directs stem cell lineage specification, Cell 126 (4) (2006) 677–689, doi:10.1016/j.cell.2006.06.044.
[5] K.A. Jansen, P. Atherton, C. Ballestrem, Mechanotransduction at the cell-matrix interface, Seminars in Cell and Developmental Biology 71 (2017) 75–83, doi:10.1016/j.semcdb.2017.07.027.
[6] M. Arnold, E.A. Cavalcanti-Adam, R. Glass, J. Blümmel, W. Eck, M. Kantlehner, H. Kessler, J.P. Spatz, Activation of integrin function by nanopatterned adhesive interfaces, Chemphyschem 5 (3) (2004) 383–388, doi:10.1002/cphc.200301014.
[7] R. Changede, H. Cai, S.J. Wind, M.P. Sheetz, Integrin nanoclusters can bridge thin matrix fibres to form cellmatrix adhesions, Nat Mater 18 (12) (2019) 1366–1375, doi:10.1038/s41563-019-0460-y.
[8] M.J. Humphries, Integrin structure, Biochem. Soc. Trans. 28 (4) (2000) 311–340, doi:10.1042/bst0280311.
[9] R. Changede, X. Xu, F. Margadant, M.P. Sheetz, Nascent integrin adhesions form on all matrix rigidities after integrin activation, Dev. Cell 35 (5) (2015) 614–621, doi:10.1016/j.devcel.2015.11.001.
[10] M. Vicente-Manzanares, A.R. Horwitz, Adhesion dynamics at a glance, J. Cell. Sci. 124 (23) (2011) 3923–3927, doi:10.1242/jcs.095653.
[11] J. Malmström, J. Lovmand, S. Kristensen, M. Sundh, M. Duch, D.S. Sutherland, Focal complex maturation and bridging on 200 nm vitronectin but not fibronectin patches reveal different mechanisms of focal adhesion formation, Nano Lett. (2011) 2264–2271, doi:10.1021/nl200447q.
[12] R.R. Besser, A.C. Bowles, A. Alassaf, D. Carbonero, I. Claure, E. Jones, J. Reda, L. Wubker, W. Batchelor, N. Ziebarth, R. Silvera, A. Khan, R. MacIel, M. Saporta, A. Agarwal, Enzymatically crosslinked gelatin-laminin hydrogels for applications in neuromuscular tissue engineering, Biomater Sci 8 (2) (2020) 591–606, doi:10.1039/c9bm01430f.
[13] S. Sainio, H. Jiang, M.A. Caro, J. Koehne, O. Lopez-Acevedo, J. Koskinen, M. Meyyappan, T. Laurila, Structural morphology of carbon nanofibers grown on different substrates, Carbon N Y 98 (2016) 343–351, doi:10.1016/j.carbon.2015.11.021.
[14] D. Sulzer, E. Kanter, Postnatal ventral midbrain dopamine neuronal culture protocols, 2011, doi:10.17504/protocols.io.bpaamiae.
[15] E.K. Dimitriadis, F. Horkay, J. Maresca, B. Kachar, R.S. Chadwick, Determination of elastic moduli of thin layers of soft material using the atomic force microscope, Biophys. J. 82 (5) (2002) 2798–2810, doi:10.1016/S0006-3495(02)75620-8.
[16] H. Hertz, Über die Berührung fester elastischer Körper (on the contact of elastic solids), Journal für die reine und angewandte Mathematik 92 (1826) 156–171.
[17] M. Glaubitz, N. Medvedev, D. Pussak, L. Hartmann, S. Schmidt, C.A. Helm, M. Delcea, A novel contact model for AFM indentation experiments on soft spherical cell-like particles, Soft Matter 10 (35) (2014) 6732–6741, doi:10.1039/c4sm00788c.
[18] K.D. Costa, Single-cell elastography: probing for disease with the atomic force microscope, Dis. Markers 19 (2–3) (2004) 139–154, doi:10.1155/2004/482680.
[19] M. Czerner, L.S. Fellay, M.P. Suárez, P.M. Frontini, L.A. Fasce, Determination of elastic modulus of gelatin gels by indentation experiments, Procedia Mater. Sci. 8 (2015) 287–296, doi:10.1016/j.mspro.2015.04.075.
[20] M. Radmacher, M. Fritz, P.K. Hansma, Imaging soft samples with the atomic force microscope: gelatin in water and propanol, Biophys. J. 69 (1) (1995) 264–270, doi:10.1016/S0006-3495(95)79897-6.
[21] C. Wei, D. Srivastava, Nanomechanics of carbon nanofibers: structural and elastic properties, Appl Phys Lett 85 (12) (2004) 2208–2210, doi:10.1063/1.1792797.
[22] I. Sneddon, The relation between load and penetration in the axisymmetric boussinesq problem for a punch of arbitrary profile, Int J Eng Sci 3 (1) (1965) 47–57, doi:10.1016/0020-7225(65)90019-4.
[23] R. Suriano, C. Credi, M. Levi, S. Turri, AFM Nanoscale indentation in air of polymeric and hybrid materials with highly different stiffness, Appl Surf Sci 311 (2014) 558–566, doi:10.1016/j.apsusc.2014.05.108.
[24] I. Sokolov, Atomic force microscopy in cancer cell research, 2007.
[25] N. Nijenhuis, X. Zhao, A. Carisey, C. Ballestrem, B. Derby, Combining AFM and acoustic probes to reveal changes in the elastic stiffness tensor of living cells, Biophys. J. 107 (7) (2014) 1502–1512, doi:10.1016/j.bpj.2014.07.073.
[26] U. Horzum, B. Ozdil, D. Pesen-Okvur, Step-by-step quantitative analysis of focal adhesions, MethodsX 1 (1) (2014) 56–59, doi:10.1016/j.mex.2014.06.004.
[27] M.F. Festing, D.G. Altman, Guidelines for the design and statistical analysis of experiments in papers submitted to ATLA, Alternatives to Laboratory Animals 29 (2001) 427–446, doi:10.1177/026119290102900409.
[28] M.F. Festing, D.G. Altman, Guidelines for the design and statistical analysis of experiments using laboratory animals, ILAR Journal 43 (4) (2002) 244–257, doi:10.1093/ilar.43.4.244.
[29] J. Fu, Y.K. Wang, M.T. Yang, R.A. Desai, X. Yu, Z. Liu, C.S. Chen, Mechanical regulation of cell function with geometrically modulated elastomeric substrates, Nat. Methods 7 (9) (2010) 733–736, doi:10.1038/nmeth.1487.
[30] A.M. Muller, D.J. Green, Elastic indentation response of float glass surfaces, J. Am. Ceram. Soc. 93 (1) (2010) 209–216, doi:10.1111/j.1551-2916.2009.03377.x.
[31] E. Martinez, J.L. Andujar, M.C. Polo, J. Esteve, J. Robertson, W.I. Milne, Study of the mechanical properties of tetrahedral amorphous carbon films by nanoindentation and nanowear measurements, Diam Relat Mater 10 (2001) 145–152.
[32] A.C. Ferrari, J. Robertson, M.G. Beghi, C.E. Bottani, R. Ferulano, R. Pastorelli, Elastic constants of tetrahedral amorphous carbon films by surface Brillouin scattering, Appl Phys Lett 75 (13) (1999) 1893–1895.
[33] M.A. Hopcroft, W.D. Nix, T.W. Kenny, What is the Young's modulus of silicon? J. Microelectromech. Syst. 19 (2) (2010) 229–238, doi:10.1109/JMEMS.2009.2039697.
[34] P. Sampath, T.D. Pollard, Effects of cytochalasin, phalloidin, and ph on the elongation of actin filaments, Biochemistry 30 (7) (1991) 1973–1980, doi:10.1021/bi00221a034.
[35] S. Köhler, K.M. Schmoller, A.H. Crevenna, A.R. Bausch, Regulating contractility of the actomyosin cytoskeleton by ph, Cell Rep 2 (3) (2012) 433–439, doi:10.1016/j.celrep.2012.08.014.
[36] T. Svitkina, The actin cytoskeleton and actin-based motility, Cold Spring Harb Perspect Biol 10 (1) (2018), doi:10.1101/cshperspect.a018267.
[37] D.E. Ingber, N. Wang, D. Stamenović, Tensegrity, cellular biophysics, and the mechanics of living systems, 2014, (????). 10.1088/0034-4885/77/4/046603
[38] N. Wang, I.M. Tolić-NØRRELYKKE, J. Chen, S.M. Mijailovich, J.P. Butler, J.J. Fredberg, D. Stamenovic, Cell prestress. i. stiffness and prestress are closely associated in adherent contractile cells, American Journal of Physology-Cell 282 (3) (2002) C606–C616, doi:10.1152/ajpcell.00269.2001.
[39] B. Geiger, K.M. Yamada, Molecular architecture and function of matrix adhesions, Cold Spring Harb Perspect Biol 3 (5) (2011) 1–21, doi:10.1101/cshperspect.a005033.
[40] S. Tojkander, G. Gateva, P. Lappalainen, Actin stress fibers - Assembly, dynamics and biological roles, J. Cell. Sci. 125 (8) (2012) 1855–1864, doi:10.1242/jcs.098087.
[41] B. Geiger, J.P. Spatz, A.D. Bershadsky, Environmental sensing through focal adhesions, Nat. Rev. Mol. Cell Biol. 10 (1) (2009) 21–33, doi:10.1038/nrm2593.
[42] C.W. Kuo, D.Y. Chueh, P. Chen, Investigation of size-dependent cell adhesion on nanostructured interfaces, J Nanobiotechnology 12 (1) (2014) 1–10, doi:10.1186/s12951-014-0054-4.
[43] J. Lee, B.S. Kang, B. Hicks, T.F. Chancellor, B.H. Chu, H.T. Wang, B.G. Keselowsky, F. Ren, T.P. Lele, The control of cell adhesion and viability by zinc oxide nanorods, Biomaterials 29 (27) (2008) 3743–3749, doi:10.1016/j.biomaterials.2008.05.029.
[44] K. Tanner, A. Boudreau, M.J. Bissell, S. Kumar, Dissecting regional variations in stress fiber mechanics in living cells with laser nanosurgery, Biophys. J. 99 (9) (2010) 2775–2783, doi:10.1016/j.bpj.2010.08.071.
[45] P.C. Georges, W.J. Miller, D.F. Meaney, E.S. Sawyer, P.A. Janmey, Matrices with compliance comparable to that of brain tissue select neuronal over glial growth in mixed cortical cultures, Biophys. J. 90 (8) (2006) 3012–3018, doi:10.1529/biophysj.105.073114.
[46] J.E. Gautrot, J. Malmström, M. Sundh, C. Margadant, A. Sonnenberg, D.S. Sutherland, The nanoscale geometrical maturation of focal adhesions controls stem cell differentiation and mechanotransduction, Nano Lett. 14 (7) (2014) 3945–3952, doi:10.1021/nl501248y.
[47] B. Zimerman, T. Volberg, B. Geiger, Early molecular events in the assembly of the focal adhesion-stress fiber complex during fibroblast spreading, Cell Motil. Cytoskeleton 58 (3) (2004) 143–159, doi:10.1002/cm.20005.
[48] F. Margadant, L.L. Chew, X. Hu, H. Yu, N. Bate, X. Zhang, M. Sheetz, Mechanotransduction in vivo by repeated talin stretch-relaxation events depends upon vinculin, PLoS Biol. 9 (12) (2011), doi:10.1371/journal.pbio.1001223.
[49] P. Kanchanawong, G. Shtengel, A.M. Pasapera, E.B. Ramko, M.W. Davidson, H.F. Hess, C.M. Waterman, Nanoscale architecture of integrin-based cell adhesions, Nature 468 (7323) (2010) 580–584, doi:10.1038/nature09621.
[50] J. Liu, Y. Wang, W.I. Goh, H. Goh, M.A. Baird, S. Ruehland, S. Teo, N. Bate, D.R. Critchley, M.W. Davidson, P. Kanchanawong, Talin determines the nanoscale architecture of focal adhesions, Proc. Natl. Acad. Sci. U.S.A. 112 (35) (2015) E4864–E4873, doi:10.1073/pnas.1512025112.
[51] J. Malmström, B. Christensen, H.P. Jakobsen, J. Lovmand, R. Foldbjerg, E.S. Sørensen, D.S. Sutherland, Large area protein patterning reveals nanoscale control of focal adhesion development, Nano Lett. 10 (2) (2010) 686–694, doi:10.1021/nl903875r.
[52] Z. Li, H. Persson, K. Adolfsson, L. Abariute, M.T. Borgström, D. Hessman, K. Åström, S. Oredsson, C.N. Prinz, Cellular traction forces: a useful parameter in cancer research, Nanoscale 9 (48) (2017) 19039–19044, doi:10.1039/c7nr06284b.
[53] L. Trichet, J. Le Digabel, R.J. Hawkins, S.R.K. Vedula, M. Gupta, C. Ribrault, P. Hersen, R. Voituriez, B. Ladoux, Evidence of a large-scale mechanosensing mechanism for cellular adaptation to substrate stiffness, Proc. Natl. Acad. Sci. U.S.A. 109 (18) (2012) 6933–6938, doi:10.1073/pnas.1117810109.
[54] S. Tavares, A.F. Vieira, A.V. Taubenberger, M. Araújo, N.P. Martins, C. Brás-Pereira, A. Polónia, M. Herbig, C. Barreto, O. Otto, J. Cardoso, J.B. Pereira-Leal, J. Guck, J. Paredes, F. Janody, Actin stress fiber organization promotes cell stiffening and proliferation of pre-invasive breast cancer cells, Nat Commun 8 (May) (2017), doi:10.1038/ncomms15237.
[55] N. Gavara, R.S. Chadwick, Relationship between cell stiffness and stress fiber amount, assessed by simultaneous atomic force microscopy and live-cell fluorescence imaging, Biomech Model Mechanobiol 15 (3) (2016) 511–523, doi:10.1007/s10237-015-0706-9.
[56] L. Bollmann, D.E. Koser, R. Shahapure, H.O. Gautier, G.A. Holzapfel, G. Scarcelli, M.C. Gather, E. Ulbricht, K. Franze, Microglia mechanics: immune activation alters traction forces and durotaxis, Front Cell Neurosci 9 (September) (2015) 1–16, doi:10.3389/fncel.2015.00363.
[57] J. Solon, I. Levental, K. Sengupta, P.C. Georges, P.A. Janmey, Fibroblast adaptation and stiffness matching to soft elastic substrates, Biophys. J. 93 (12) (2007) 4453–4461, doi:10.1529/biophysj.106.101386.

[58] E.Y. Yukako, S. Hatsuki, H. Hisashi, K. Kazushige, A. Kazuhiro Ito, Quantitative analyses of topography and elasticity of living and fixed astrocytes, J Electron Microsc (Tokyo) 49 (3) (2000) 463–471, doi:10.1093/oxfordjournals.jmicro.a023830.
[59] J.C. Gil-Redondo, J. Iturri, F. Ortega, R. Pérez-Sen, A. Weber, M.T. Miras-Portugal, J.L. Toca-Herrera, E.G. Delicado, Nucleotides-induced changes in the mechanical properties of living endothelial cells and astrocytes, analyzed by atomic force microscopy, Int J Mol Sci 22 (2) (2021) 1–18, doi:10.3390/ijms22020624.
[60] T.G. Kuznetsova, M.N. Starodubtseva, N.I. Yegorenkov, S.A. Chizhik, R.I. Zhdanov, Atomic force microscopy probing of cell elasticity, Micron 38 (8) (2007) 824–833, doi:10.1016/j.micron.2007.06.011.
[61] W.J. Miller, I. Leventhal, D. Scarsella, P.G. Haydon, P. Janmey, D.F. Meaney, Mechanically induced reactive gliosis causes ATP-mediated alterations in astrocyte stiffness, J. Neurotrauma 26 (5) (2009) 789–797, doi:10.1089/neu.2008.0727.
[62] D. Vergara, R. Martignago, S. Leporatti, S. Bonsegna, G. Maruccio, F.D. Nuccio, A. Santino, R. Cingolani, G. Nicolardi, M. Maffia, R. Rinaldi, Biomechanical and proteomic analysis of INF- β-treated astrocytes, Nanotechnology 20 (45) (2009), doi:10.1088/0957-4484/20/45/455106.
[63] N. Curry, G. Ghézali, G.S. Schierle, N. Rouach, C.F. Kaminski, Correlative STED and atomic force microscopy on live astrocytes reveals plasticity of cytoskeletal structure and membrane physical properties during polarized migration, Front Cell Neurosci 11 (April) (2017) 1–10, doi:10.3389/fncel.2017.00104.
[64] T.D. Nguyen, Y. Gu, Exploration of mechanisms underlying the strain-rate-dependent mechanical property of single chondrocytes, Appl Phys Lett 104 (18) (2014) 1–5, doi:10.1063/1.4876056.
[65] A. Weber, J. Iturri, R. Benitez, J.L. Toca-Herrera, Measuring biomaterials mechanics with atomic force microscopy. 1. influence of the loading rate and applied force (pyramidal tips), Microsc. Res. Tech. 82 (9) (2019) 1392–1400, doi:10.1002/jemt.23291.
[66] K. Mollaeian, Y. Liu, S. Bi, J. Ren, Atomic force microscopy study revealed velocity-dependence and nonlinearity of nanoscale poroelasticity of eukaryotic cells, J Mech Behav Biomed Mater 78 (May 2017) (2018) 65–73, doi:10.1016/j.jmbbm.2017.11.001.
[67] P. Moshayedi, L. Da F Costa, A. Christ, S.P. Lacour, J. Fawcett, J. Guck, K. Franze, Mechanosensitivity of astrocytes on optimized polyacrylamide gels analyzed by quantitative morphometry, Journal of Physics Condensed Matter 22 (19) (2010), doi:10.1088/0953-8984/22/19/194114.
[68] J.P. Califano, C.A. Reinhart-King, Substrate stiffness and cell area predict cellular traction stresses in single cells and cells in contact, Cell Mol Bioeng 3 (1) (2010) 68–75, doi:10.1007/s12195-010-0102-6.
[69] J. Stricker, T. Falzone, M.L. Gardel, Mechanics of the F-actin cytoskeleton, J Biomech 43 (1) (2010) 9–14, doi:10.1016/j.jbiomech.2009.09.003.
[70] S. Hu, J. Chen, N. Wang, Physiology program, department of environmental health, harvard school of public health, boston, MA 02115, Frontiers in Bioscience 9 (3) (2004) 2177–2182, doi:10.2741/1352.
[71] S. Kaech, G. Banker, Culturing hippocampal neurons, Nat Protoc 1 (5) (2006) 2406–2415, doi:10.1038/nprot.2006.356.
[72] Y. Zhang, B. Zhu, F. Ma, K. Herrup, Identifying a population of glial progenitors that have been mistaken for neurons in embryonic mouse cortical culture, eNeuro 8 (2) (2021) 1–12, doi:10.1523/ENEURO.0388-20.2020.
[73] P.J. Darlington, J.S. Goldman, Q.L. Cui, J.P. Antel, T.E. Kennedy, Widespread immunoreactivity for neuronal nuclei in cultured human and rodent astrocytes, J. Neurochem. 104 (5) (2008) 1201–1209, doi:10.1111/j.1471-4159.2007.05043.x.
[74] R.T. Fremeau, M.D. Troyer, I. Pahner, G.O. Nygaard, C.H. Tran, R.J. Reimer, E.E. Bellocchio, D. Fortin, J. Storm-Mathisen, R.H. Edwards, The expression of vesicular glutamate transporters defines two classes of excitatory synapse, Neuron 31 (2) (2001) 247–260, doi:10.1016/S0896-6273(01)00344-0.
[75] E. Biffi, G. Regalia, A. Menegon, G. Ferrigno, A. Pedrocchi, The influence of neuronal density and maturation on network activity of hippocampal cell cultures: a methodological study, PLoS ONE 8 (12) (2013), doi:10.1371/journal.pone.0083899.
[76] M.V. Accardi, M.K. Pugsley, R. Forster, E. Troncy, H. Huang, S. Authier, The emerging role of in vitro electrophysiological methods in CNS safety pharmacology, J Pharmacol Toxicol Methods 81 (2016) 47–59, doi:10.1016/j.vascn.2016.03.008.
[77] M. Meijer, K. Rehbach, J.W. Brunner, J.A. Classen, H.C. Lammertse, L.A. van Linge, D. Schut, T. Krutenko, M. Hebisch, L.N. Cornelisse, P.F. Sullivan, M. Peitz, R.F. Toonen, O. Brüstle, M. Verhage, A single-Cell model for synaptic transmission and plasticity in human iPSC-derived neurons, Cell Rep 27 (7) (2019) 2199–2211.e6, doi:10.1016/j.celrep.2019.04.058.
[78] R.T. Roppongi, K.P. Champagne-Jorgensen, T.J. Siddiqui, Low-density primary hippocampal neuron culture, Journal of Visualized Experiments 2017 (122) (2017) 1–7, doi:10.3791/55000.
[79] S. LuZhongming; Piechowicz,Mariel; Qiu, A simplified method for ultra-low density, long-Term primary hippocampal neuron culture, Journal of Visualized Experiments 109 (2016) e53797, doi:10.3791/53797.
[80] Y.W. Fan, F.Z. Cui, S.P. Hou, Q.Y. Xu, L.N. Chen, I.S. Lee, Culture of neural cells on silicon wafers with nano-scale surface topograph, J. Neurosci. Methods 120 (1) (2002) 17–23, doi:10.1016/S0165-0270(02)00181-4.
[81] K.V. Brix, C.E. Schlekat, E.R. Garman, The mechanisms of nickel toxicity in aquatic environments: an adverse outcome pathway analysis, Environ. Toxicol. Chem. 36 (5) (2017) 1128–1137, doi:10.1002/etc.3706.
[82] K. Jomova, S. Baros, M. Valko, Redox active metal-induced oxidative stress in biological systems, Transition Met. Chem. 37 (2) (2012) 127–134, doi:10.1007/s11243-012-9583-6.
[83] K.E. Heim, R. Danzeisen, V. Verougstraete, F. Gaidou, T. Brouwers, A.R. Oller, Bioaccessibility of nickel and cobalt in synthetic gastric and lung fluids and its potential use in alloy classification, Regul. Toxicol. Pharm. 110 (May 2019) (2020) 104549, doi:10.1016/j.yrtph.2019.104549.
[84] S. Sainio, D. Nordlund, R. Gandhiraman, H. Jiang, J. Koehne, J. Koskinen, M. Meyyappan, T. Laurila, What does nitric acid really do to carbon nanofibers? J. Phys. Chem. C 120 (39) (2016) 22655–22662, doi:10.1021/acs.jpcc.6b06353.
[85] S. Desagher, J. Glowinski, J. Premont, Astrocytes protect neurons from hydrogen peroxide toxicity, J. Neurosci. 16 (8) (1996) 2553–2562, doi:10.1523/jneurosci.16-08-02553.1996.
[86] Y. Chen, C. Qin, J. Huang, X. Tang, C. Liu, K. Huang, J. Xu, G. Guo, A. Tong, L. Zhou, The role of astrocytes in oxidative stress of central nervous system: a mixed blessing, Cell Prolif. 53 (3) (2020) 1–13, doi:10.1111/cpr.12781.
[87] G.J. Kress, K.E. Dineley, I.J. Reynolds, The relationship between intracellular free iron and cell injury in cultured neurons, astrocytes, and oligodendrocytes, J. Neurosci. 22 (14) (2002) 5848–5855, doi:10.1523/jneurosci.22-14-05848.2002.
[88] T. Roitbak, E. Syková, Diffusion barriers evoked in the rat cortex by reactive astrogliosis, Glia 28 (1) (1999) 40–48, doi:10.1002/(SICI)1098-1136(199910)28:1<40::AID-GLIA5>3.0.CO;2-6.
[89] S.M. Wellman, T.D. Kozai, Understanding the inflammatory tissue reaction to brain implants to improve neurochemical sensing performance, ACS Chem Neurosci 8 (12) (2017) 2578–2582, doi:10.1021/acschemneuro.7b00403.
[90] Z. Yu, T.E. McKnight, M.N. Ericson, A.V. Melechko, M.L. Simpson, B. Morrison, Vertically aligned carbon nanofiber arrays record electrophysiological signals from hippocampal slices, Nano Lett. 7 (8) (2007) 2188–2195, doi:10.1021/nl070291a.
[91] S. Sainio, T. Palomäki, N. Tujunen, V. Protopopova, J. Koehne, K. Kordas, J. Koskinen, M. Meyyappan, T. Laurila, Integrated carbon nanostructures for detection of neurotransmitters, Mol. Neurobiol. 52 (2) (2015) 859–866, doi:10.1007/s12035-015-9233-z.
[92] N. Isoaho, E. Peltola, S. Sainio, J. Koskinen, T. Laurila, Pt-grown carbon nanofibers for enzymatic glutamate biosensors and assessment of their biocompatibility, RSC Adv 8 (62) (2018) 35802–35812, doi:10.1039/C8RA07766E.
[93] P.J. Grahn, G.W. Mallory, O.U. Khurram, B.M. Berry, J.T. Hachmann, A.J. Bieber, K.E. Bennet, H.K. Min, S.Y. Chang, K.H. Lee, J.L. Lujan, A neurochemical closed-loop controller for deep brain stimulation: toward individualized smart neuromodulation therapies, Front Neurosci 8 (8 JUN) (2014) 1–11, doi:10.3389/fnins.2014.00169.
[94] J.G. Habets, M. Heijmans, M.L. Kuijf, M.L. Janssen, Y. Temel, P.L. Kubben, An update on adaptive deep brain stimulation in Parkinson's disease, Movement Disorders 33 (12) (2018) 1834–1843, doi:10.1002/mds.115.